Physics of the Earth and Planetary Interiors 266 (2017) 39–53

Contents lists available at ScienceDirect

Physics of the Earth and Planetary Interiors

journal homepage: www.elsevier.com/locate/pepi

Relating the South Atlantic Anomaly and geomagnetic flux patches

Filipe Terra-Nova [a,*], Hagay Amit [a], Gelvam A. Hartmann [b], Ricardo I.F. Trindade [c], Katia J. Pinheiro [d]

[a] CNRS, Université de Nantes, Nantes Atlantiques Universités, UMR CNRS 6112, Laboratoire de Planétologie et de Géodynamique, 2 rue de la Houssinière, F-44000 Nantes, France
[b] Instituto de Geociências, Universidade Estadual de Campinas, Rua João Pandiá Calógeras, 51, 13083-870 Campinas, Brazil
[c] Departamento de Geofísica, Instituto de Astronomia, Geofísica e Ciências Atmosféricas, Universidade de São Paulo, Rua do Matão, 1226, Cidade Universitária, 05508-090 São Paulo, Brazil
[d] Observatório Nacional, Rua General José Cristino, 77, 20921-400 Rio de Janeiro, Brazil

ARTICLE INFO

Article history:
Received 3 October 2016
Received in revised form 13 January 2017
Accepted 6 March 2017
Available online 8 March 2017

Keywords:
South Atlantic Anomaly
Geomagnetic flux patches
Axial dipole
Core-mantle boundary
Kernel functions
Secular variation

ABSTRACT

The South Atlantic Anomaly (SAA) is a region of weak geomagnetic field intensity at the Earth's surface, which is commonly attributed to reversed flux patches (RFPs) on the core-mantle boundary (CMB). While the SAA is clearly affected by the reversed flux region below the South Atlantic, we show that the relation between the intensity minimum at Earth's surface and RFPs is not straightforward. We map a field-dependent intensity kernel (Constable, 2007a) to study the relation between the radial geomagnetic field at the CMB and the field intensity at Earth's surface. Synthetic tests highlight the role of specific patches (reversed and normal) in determining the location of the surface intensity minimum and demonstrate that the SAA can indeed be explained by a few intense patches. We show that the level of axial dipolarity of the field determines the stability of the relation between the SAA minimum and RFPs. The present position of the SAA minimum is determined by the interplay among several robust geomagnetic flux patches at the CMB. The longitude of the SAA minimum appears near the longitude of the Patagonia RFP due to the low-latitude normal flux patches (NFPs) near Africa and mid-Atlantic which diminish the effect of the Africa RFPs. The latitude of the SAA minimum is lower than the Patagonia RFP latitude due to the South Pacific high-latitude NFP and the axial dipole effect. The motion of the SAA minimum is explained by the motions and changes in intensity of these robust geomagnetic flux patches. Simple secular variation (SV) scenarios suggest that while the SAA path can be explained by advection, its intensity decrease requires magnetic diffusion. In addition these SV scenarios provide some speculative predictions for the SAA.

1. Introduction

The South Atlantic Anomaly (SAA) is a region where the lowest geomagnetic field intensity values at the Earth's surface are observed. It is one of the most important features of the Earth's surface field where a strong non-dipolar field is present (Hartmann and Pacca, 2009). The SAA minimum intensity is currently located at inland South Brazil (Thébault et al., 2015). It has been decreasing with time (Hartmann and Pacca, 2009; Finlay et al., 2010), in conjunction with the rapidly decreasing geomagnetic dipole intensity (e.g. Finlay, 2008). The decreasing dipole is in part associated to the proliferation of reversed flux patches (RFPs) below the South Atlantic and their poleward motion (e.g. Gubbins, 1987; Hulot et al., 2002; Olson and Amit, 2006; Finlay et al., 2012, 2016; Terra-Nova et al., 2015). The SAA has been commonly attributed to RFPs at the core-mantle boundary (CMB) (e.g. Tarduno et al., 2015) . Changes in the SAA position and intensity are intrinsically related to the flow patterns at the top of the core especially near RFPs (Aubert, 2015).

RFPs may emerge by expulsion of toroidal field lines due to fluid upwelling at the top of the core (Bloxham, 1986), therefore RFPs may be paired with normal flux patches (NFPs) (Jackson, 2003; Terra-Nova et al., 2016). Recently, Finlay et al. (2016) combined observed field models and equatorially symmetric core flow models to show that an RFP located below Patagonia breaks the symmetry of advective sources of the axial dipole moment (ADM) changes thus causing its decrease. Although Olson and Amit (2006) used a distinctive helical core flow model, they also found a similar pattern of advective ADM sources with symmetry breaking below South America. We will show that the Patagonia RFP also determines the longitude of the SAA minimum because this patch does not pair with a low-latitude NFP.

The SAA persistence is under debate. Aubert (2015) obtained geomagnetic forecasting based on a data assimilation technique that relies on statistical properties of a numerical dynamo model

* Corresponding author.
E-mail address: filipe.terranova@univ-nantes.fr (F. Terra-Nova).

http://dx.doi.org/10.1016/j.pepi.2017.03.002
0031-9201/

that reproduces some robust historical field and secular variation (SV) features. He predicted that the SAA will drift westward to eastern Pacific Ocean until 2115. Based on local field intensity measurements of African artefacts, Tarduno et al. (2015) argued for persistent recurrence of low field intensity associated to the SAA. They suggested that the SAA location is ancient due to prescribed positions of RFPs below Africa which are controlled by the heterogeneous lower mantle. Overall, it is under debate whether the current location of the SAA is quasi-stationary (due to boundary control) or strongly transient. While the SAA position is clearly affected by the reversed flux region below the South Atlantic, we will show that relating the SAA minimum to RFPs is not trivial.

Previous studies related the surface components of Earth's magnetic field and the radial field at the CMB via kernel functions (e.g. Gubbins and Roberts, 1983; Johnson and Constable, 1997; Gubbins, 2004; Constable, 2007a). Johnson and Constable (1997) derived field-dependent kernel functions for declination and inclination to study the effect of low geomagnetic data coverage on global modeling. These methodologies provide the tools to derive a field-dependent kernel function to relate the radial field at the CMB to the surface intensity field (Constable, 2007a). In particular, this intensity kernel may be applied as an analytical tool to study the relation between the radial field at the CMB and the SAA.

Based on kernel functions, Chulliat et al. (2010) studied the relation between RFPs at the CMB to magnetic pole motion at Earth's surface. Such a formalism has not yet been applied for the relation between RFPs at the CMB and the minimum intensity of the surface field as observed in the SAA region. Tracking of the SAA minimum was performed at Earth's surface (Hartmann and Pacca, 2009; Finlay et al., 2010; Aubert, 2015), and tracking of RFPs was performed at the CMB (Terra-Nova et al., 2015, 2016), but the relation between the SAA and RFPs has not been demonstrated. In this study, we use historical and modern geomagnetic field models to unravel the relations between geomagnetic flux patches and the SAA minimum location, motion and intensity changes.

2. Theory and methods

2.1. Kernels

To generally assess how the radial magnetic field at a given point at the CMB affects the field at a given point above the CMB we consider appropriate kernel functions (Gubbins and Roberts, 1983; Constable et al., 1993; Johnson and Constable, 1997). The following equation reconstructs the field at the position vector from Earth's center **r**:

$$\mathbf{B}(\mathbf{r}) = \int_S \mathbf{G}(\mathbf{r}|\hat{s}) B_r(c, \phi', \theta') \sin\theta' \mathrm{d}\phi' \mathrm{d}\theta' \tag{1}$$

where $\mathbf{G}(\mathbf{r}|\hat{s})$ contains the kernel functions relating the CMB radial field B_r with the field vector **B** at **r**, c is the CMB radius, S is the CMB surface and $\hat{s}$ is its normal unit vector. The pairs $(\phi,\ \theta)$ and $(\phi',\ \theta')$ represent the position (longitude, colatitude) of a given point at **r** and at the CMB, respectively. The kernel function $G(\mu)$ for the Neumann problem in Laplace's equation is (Mikhlin, 1970):

$$G(\mu) = \frac{c}{4\pi}\left(ln\left(\frac{f + x - \mu}{1 - \mu}\right) - \frac{2x}{f}\right) \tag{2}$$

where $x = c/r$, r is the radial distance, $f = (1 - 2x\mu + x^2)^{1/2}$ and $\mu = \cos\alpha$ where α is the angle between the points $(\phi,\ \theta)$ and $(\phi',\ \theta')$.

The kernel function for the radial field at Earth's surface (Gubbins and Roberts, 1983) is

$$G_r = \left(\frac{dG}{dr}\right)_{r=a} = \frac{b^2(1 - b^2)}{4\pi f^3} \tag{3}$$

where $b = c/a$ and a is Earth's radius. The kernel functions for the horizontal vector field components are

$$G_\theta = \frac{1}{r}\frac{\partial G}{\partial \mu}\frac{\partial \mu}{\partial \theta} = \frac{1}{r}\frac{\partial G}{\partial \mu}(cos\theta sin\theta' cos(\phi - \phi') - sin\theta cos\theta') \tag{4}$$

$$G_\phi = \frac{1}{r}\frac{\partial G}{\partial \mu}\frac{1}{sin\theta}\frac{\partial \mu}{\partial \phi} = -\frac{1}{r}\frac{\partial G}{\partial \mu}(sin\theta' sin(\phi - \phi')) \tag{5}$$

where

$$\frac{1}{r}\frac{\partial G}{\partial \mu} = -\frac{x}{4\pi}\left(\frac{1 - 2x\mu + 3x^2}{f^3} + \frac{\mu}{f(f + x - \mu)} - \frac{1}{(1 - \mu)}\right) \tag{6}$$

Note that (4) and (5) depend on several functions of $(\phi,\ \theta,\ \phi',\ \theta')$ and thus cannot be expressed exclusively as a function of μ. However, a kernel function for the horizontal field can be expressed exclusively by μ (for details see e.g. Gubbins and Roberts, 1983):

$$G_h = (1 - \mu^2)^{1/2}\left(\frac{1}{r}\frac{\partial G}{\partial \mu}\right)_{r=a} \tag{7}$$

Fig. 1 shows G_r and G_h as functions of μ as well as G_θ and G_ϕ for an arbitrary surface point at $(0^\circ,\ 90^\circ)$. G_r and G_h have maxima at $\mu = 1$ and $\mu = 0.92$, corresponding to $\alpha = 0^\circ$ (i.e exactly beneath $(\phi,\ \theta)$) and $\alpha = 23^\circ$, respectively (e.g. Gubbins, 2004). G_θ and G_ϕ have a more complex configuration with extrema 23° away from the surface point north/south and east/west, respectively. G_θ and G_ϕ have negative values which modulate the signal to their respective influenced surface components, unlike G_h and G_r that are positive everywhere.

Since we wish to find the relation between CMB features and the surface intensity, a kernel function that relates the radial field at the CMB to the field intensity at the surface is needed. Following Johnson and Constable (1997) the intensity kernel is

$$G_F = \frac{\partial F}{\partial B_r} = \frac{1}{F}(B_\theta(a)G_\theta + B_\phi(a)G_\phi + B_r(a)G_r) \tag{8}$$

where B_θ, B_ϕ, and B_r are the surface field components pointing to South, East and outward from the Earth's surface respectively, and the surface field intensity is $F = \sqrt{B_\theta^2 + B_\phi^2 + B_r^2}$. It is worth noting that G_F also depends on the surface field components, unlike G_θ, G_ϕ, G_r and G_h that depend only on the geometry between CMB and surface points. Because F is non-linear to B_r, it cannot be reconstructed by an analogous equation to (1). The kernel (8) reflects the sensitivity of the surface intensity to changes in the radial field on the CMB about a given background field.

2.2. Identification

Previous studies characterized the SAA by an area at Earth's surface bounded by a certain low field intensity value (e.g. Pavón-Carrasco and De Santis, 2016). Such a measure is indeed relevant for spacecraft failures. We characterize the SAA by the point of minimum intensity (as in e.g. Hartmann and Pacca, 2009; Finlay et al., 2010; Aubert, 2015). Although our measure is not directly related to spacecraft safety, it does not rely on an arbitrary threshold and it allows for temporal tracking which provides direct insight to core dynamics. Overall, the time-evolution of the minimum intensity and the size of the area below an intensity threshold are well anti-correlated (Pavón-Carrasco and De Santis, 2016) so in practice the location of the minimum intensity as well as its value provide a satisfactory description of the SAA.

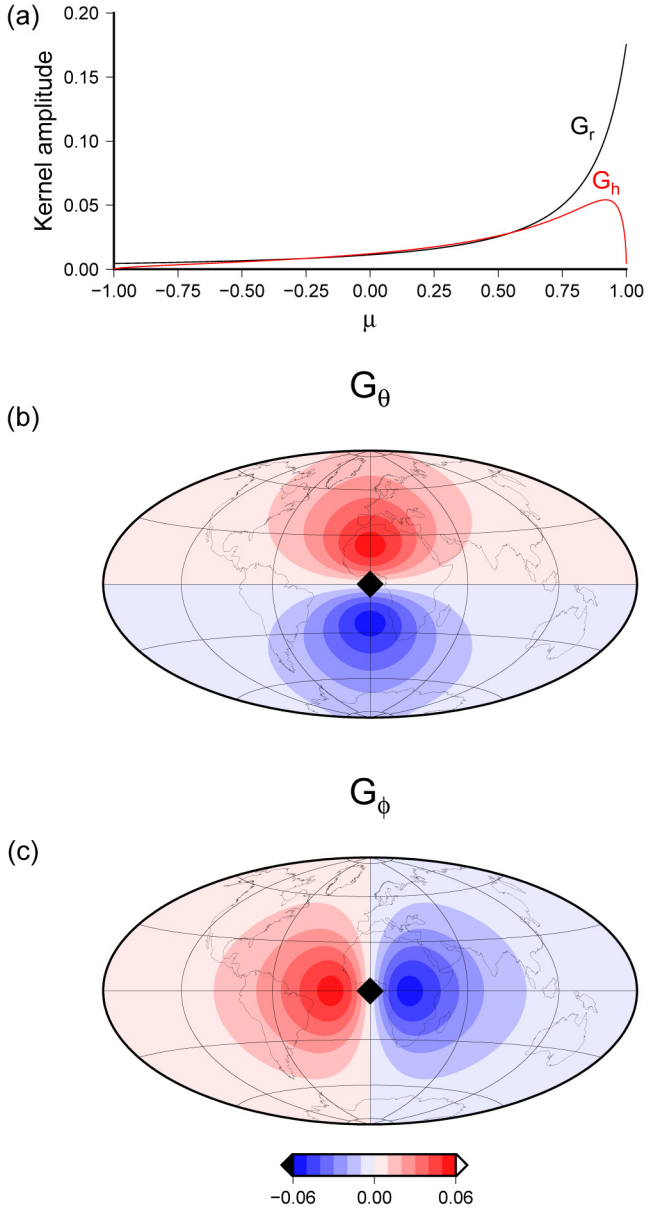

Fig. 1. (a): Kernels G_r and G_h (black and red lines, respectively) as functions of $\mu = cos\alpha$. (b) and (c): Kernels G_θ and G_ϕ, respectively, with black diamonds indicating the surface point for which the kernels are calculated. (For interpretation of the references to colour in this figure legend, the reader is referred to the web version of this article.)

We perform two steps to identify the position of the SAA minimum. First, we locate the minimum value of the field intensity on a spherical surface of a $1^\circ \times 1^\circ$ regular grid. Second, we interpolate this grid point and its near neighbors using a second degree 2D polynomial function in longitude and latitude.

To identify RFPs at the CMB snapshots we used the same topological algorithms of Terra-Nova et al. (2015), with one adjustment. Here we use a stronger intensity criterion, due to the higher spatial resolution of the historical and modern field models compared to that of the archeomagnetic field models for which the algorithms were originally designed, in order to filter out the more abundant weak RFPs in the historical and modern field models. Only RFPs with peak values larger than 0.6 of the most intense RFP of the same snapshot pass the criterion. As in Terra-Nova et al. (2016) we adjust these algorithms to also identify NFPs using a stronger intensity threshold of 0.75.

3. Synthetic tests

Intense geomagnetic flux patches at the CMB (Christensen et al., 2010) which are observed in historical field models (Jackson, 2003) are also robust features of the field on millennial timescales (Amit et al., 2011; Terra-Nova et al., 2015, 2016) and possibly on much longer timescales as well (Kelly and Gubbins, 1997; Constable, 2007b). Their surface expression is not trivial due to the mixing of upward continued spherical harmonic contributions. To gain insight into the role of such patches in localizing the minimum intensity at the Earth's surface, we performed several synthetic tests of simple radial magnetic field configurations to guide us in the interpretation of field models based on observations. We built synthetic radial magnetic fields from a background axial dipole field B_r^D superimposed by several localized flux patches. This background field is essential to define the polarity of each patch (normal or reversed). The actual dipole is a sum of the background dipole and the dipole associated with the patches. For each synthetic model we calculated the Earth's surface intensity and identified its minimum (or in some cases minima).

Following Amit (2014), the radial field of a synthetic intense magnetic flux patch was modeled as a 2D isotropic Gaussian:

$$B_r^p = A_0\left(\frac{1}{\sqrt{2\pi\sigma^2}}e^{-\frac{d^2}{2\sigma^2}}\right), \tag{9}$$

where A_0 is the amplitude corresponding to the radial field peak at the center of the patch, d is the great circle distance from the center of the magnetic flux patch to a point at the CMB and σ is the standard deviation which characterizes the width of the patch. The amplitude and the width are chosen to roughly mimic the morphology of Earth-like patches (Amit, 2014). The synthetic field $B_r(\phi,\ \theta)$ is then given by:

$$B_r(\phi,\ \theta) = B_r^D(\theta) + \sum_i (B_r^p(\phi,\ \theta))_i, \tag{10}$$

where i denotes summation over multiple patches. The widths are identical for all patches except for the cases that simulate the effect of magnetic field stretching. The amplitudes of the patches were set to maintain $\int_S B_r dS = 0$.

3.1. Minimum surface intensity and core-mantle boundary patches

For fundamental understanding, as a first step we built eight different synthetic radial magnetic fields to study the relation between the positions of patches at the CMB and the position of the minimum field intensity point at the Earth's surface F_{min}. The synthetic fields setups are summarized in Table 1. The results of the synthetic tests, including the position and the intensity of F_{min}, the area of weak intensity and the axial dipole of the synthetic fields are also given in Table 1. Since the intensity is affected by the axial dipole, we calculated a relative value of minimum intensity normalized by that of the background axial dipole contribution F_{min}/F_{min}^D (F_{min}^D is identical for cases 1–8). The closer this ratio is to unity the lower the influence of the synthetic patches on the F_{min} value. Likewise we monitored the relative axial dipole m_z/m_z^D. Lastly, we quantified the area of weak surface intensity $\mathcal{A}$ which we defined as the portion of Earth's surface with intensity values lower than $1.2F_{min}$ for each case. Smaller area corresponds to a sharper depression of surface intensity morphology, i.e. higher field roughness.

Fig. 2 shows the synthetic field models at the CMB and their intensity at the Earth's surface for cases 1, 2, 4 and 8. Case 1 has an RFP at each hemisphere both centered at latitudes 30° with an offset of 120° longitude between them. It results in two F_{min} with longitudes determined by the RFPs, but their latitudes are

Table 1
Synthetic fields setup and minimum intensity point at the Earth's surface (F_{min}).

Case	Setup				Results				
	ϕ_p	λ_p	Amp.	Flux	m_z/m_z^D	$\phi_{F_{min}}$	$\lambda_{F_{min}}$	F_{min}/F_{min}^D	$\mathcal{A}$
1	−120	−30	A_0	R	0.95	−120	−9	0.85	25.7%
	120	30	A_0	R		120	9	0.85	25.7%
2	−120	−30	A_0	R	1.00	−118	−8	0.88	17.2%
	120	−30	A_0	N					
3	−120	−60	A_0	N	1.02	118	−8	0.89	19.1%
	120	−30	A_0	R					
4	−120	−30	A_0	R	1.02	−120	−4	0.94	30.0%
	−120	−60	A_0	N					
5	−120	−45	A_0	R	1.01	−119	−3	0.97	34.6%
	−120	−60	A_0	N					
6	−120	−30	A_0	N	1.05	0	0	1.02	31.6%
	120	30	A_0	N					
7	−120	−30	$2A_0$	R	0.90	−119	−14	0.75	14.0%
	120	30	$2A_0$	R		119	14	0.75	14.0%
8	−120	−30	$2A_0$	R	1.08	117	−11	0.84	7.8%
	−120	−60	$4A_0$	N					
	120	−30	$2A_0$	R					
9	−60	−30	A_0	R	1.31	−46	−6	1.08	15.7%
	60	−30	A_0	R					
	−120	−60	$2A_0$	N					
	−120	60	$2A_0$	N					
	120	−60	$2A_0$	N					
	120	60	$2A_0$	N					
	60	0	$2A_0$	N					
10	As case 9				2.04	−37	−9	1.35	8.7%
11	−60	−30	A_0	R	1.88	−54	−13	1.24	4.1%
	60	−30	A_0	R					
	−120	−60	A_0	N					
	−120	60	$2A_0$	N					
	120	−60	$2A_0$	N					
	120	60	$2A_0$	N					
	60	0	$2A_0$	N					
	0	0	A_0	N					
12	−60	−45	A_0	R	1.86	−57	−22	1.11	3.3%
	60	−30	A_0	R					
	−120	−60	A_0	N					
	−120	60	$2A_0$	N					
	120	−60	$2A_0$	N					
	120	60	$2A_0$	N					
	60	0	$2A_0$	N					
	0	0	A_0	N					
Earth	CHAOS5 – 2003				–	−55	−26	–	8.4%

ϕ_p is patch longitude, λ_p is patch latitude, Amp. is amplitude and R and N indicate if the flux patch is reversed or normal, respectively. m_z is the axial dipole moment, whilst m_z^D is the axial dipole moment of the background field. $\phi_{F_{min}}$ is F_{min} longitude, $\lambda_{F_{min}}$ is F_{min} latitude, F_{min}/F_{min}^D is the minimum field intensity normalized by the minimum due only to the background field. $\mathcal{A}$ is the percentage of Earth's surface area that contains intensity values lower than $1.2F_{min}$. In cases 10–12 the background axial dipole field is reduced by 70%.

$\sim 21^\circ$ lower; without patches, both the magnetic equator and F_{min} appear at the geographic equator (axial dipole effect). Case 2 has an RFP and an NFP in the Southern Hemisphere, again at latitude 30° with an offset of 120° longitude between them. The RFP determines the longitude of F_{min} while the NFP determines the longitude of the maximum intensity along the equator. The latitude of F_{min} is once again lowered by the axial dipole effect. Case 4 also has an RFP and an NFP in the Southern Hemisphere, but at the same longitude, with the NFP at a higher latitude. The F_{min} longitude is again determined by the RFP, but the proximity of the NFP reduces the F_{min} latitude with respect to that of case 2. Case 8 has two RFPs and an NFP in the Southern Hemisphere, the twice stronger NFP amplitude balancing that of the RFPs. The RFPs are in the same locations as the patches in case 2, and the NFP appears in the same longitude of one RFP but at a higher latitude. The RFP which does not pair with the NFP dictates the longitude of the F_{min}. Again latitude reduction is associated to the axial dipole effect.

In almost all cases 1–8 the longitude of F_{min} is determined by the longitude of RFPs. An exception is case 6 that does not contain RFPs. In this case the longitudinal position of the minimum field intensity is farthest from the NFPs (Table 1). Indeed in all cases F_{min} tends to be far from NFPs.

In all cases F_{min} is closer to the equator than to the RFPs. Cases 2–5 have two patches in the Southern Hemisphere, one RFP and one NFP. In cases 2 and 3 these patches have different longitudes, for case 2 the same latitude and for case 3 the NFP is at higher latitude. In both cases the F_{min} latitude is the same, i.e. the latitude of the far NFP has little effect on the location of the F_{min}. Cases 4 and 5 have RFP and NFP in the same longitude, with the RFP closer to the equator than the NFP. The F_{min} is closer to the equator than in cases 2 and 3, thus the proximity of the NFP appears to reduce the F_{min} latitude. Comparing cases 4 and 5 we observe that the F_{min} latitude is closer to the equator in the latter (where the RFP is at higher latitude) because the proximity of NFP to RFP reduces the RFP effect.

Case 7 is set as case 1 but with twice stronger RFPs amplitudes. This case has the lowest value of the ratio m_z/m_z^D (Table 1) and F_{min} is farthest from the equator, demonstrating the competition between the patches and the axial dipole in determining the latitude of F_{min}. Case 7 also has the lowest F_{min}/F_{min}^D value, further demonstrating how strong RFPs can efficiently diminish locally

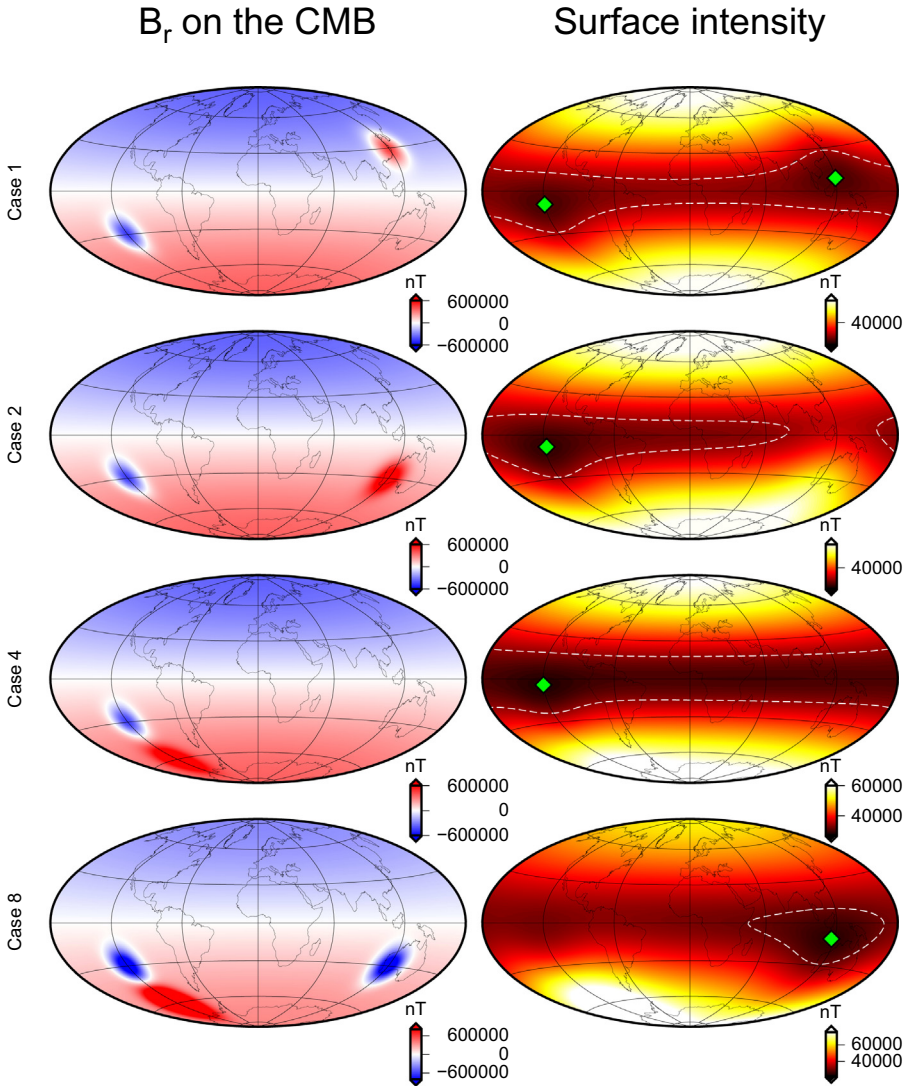

Fig. 2. Synthetic radial magnetic fields at the CMB (left) and intensity at Earth's surface (right) for cases 1, 2, 4 and 8 (see Table 1). The F_{min} locations are denoted by green diamonds (right). The area of weak intensity (delimited by the $1.2F_{min}$ contour) is denoted by a white dashed line. (For interpretation of the references to colour in this figure legend, the reader is referred to the web version of this article.)

the surface field intensity. Several cases may suggest that m_z/m_z^D and F_{min}/F_{min}^D are related. However, cases 3 and 4 have the same m_z/m_z^D but F_{min}/F_{min}^D is lower in case 3 since the NFP is not in the same longitude of the RFP as in case 4. Case 6 has F_{min}/F_{min}^D larger than 1. In this case, in the absence of RFPs, NFPs enhance the F_{min} value beyond the background field, i.e. the F_{min} is located where the influence of the NFPs is the lowest. In case 8 the strong NFP gives a large m_z/m_z^D and the strong RFP gives a low F_{min}/F_{min}^D. Overall, the lowest values of F_{min}/F_{min}^D were associated to large amplitude RFPs (cases 7 and 8).

Case 8 with higher amplitude patches shows strong local effects, as evidenced in its smallest weak intensity area $\mathcal{A}$ (see also case 7). Larger $\mathcal{A}$ is associated to the proximity between RFPs and NFPs (cases 4 and 5) or absence of RFPs (case 6). Lastly, we also show in Table 1 results of F_{min} based on the geomagnetic field model CHAOS5 (Finlay et al., 2015) at 2003 expanded until spherical harmonic degree 14. Its F_{min} is at a relatively high latitude 26° indicating strong RFPs effect. In addition, the small $\mathcal{A}$ value is associated with a rather sharp area morphology as expected from the complex field.

3.2. Towards more realistic field morphology

Next we incorporate in our synthetic models some main features that are present in the current geomagnetic field (see section 4) in order to improve our understanding of the relation between CMB patches and the F_{min} at more realistic conditions. In particular, as shown above, while recovering the SAA longitude appears to be feasible, the latitude seems more elusive. We built a series of field models (cases 9–12 in Table 1) that progressively add main features of the geomagnetic field in order to approach the SAA position.

Starting from case 9, we present a first attempt to get somewhat closer to the distribution of the more prominent geomagnetic flux patches, but still within a synthetic framework that allows understanding of the role of each patch. This synthetic field comprises four high-latitude NFPs (two at each hemisphere) and one equatorial NFP, as well as two RFPs in the Southern Hemisphere. The RFPs are at latitudes 30° and longitudes ±60°, while the high-latitude NFPs (all at latitudes 60°) form two pairs of same longitude in opposite hemispheres at longitudes ±120° (Fig. 3). The equatorial NFP is located at the same longitude as one of the RFPs. The result-

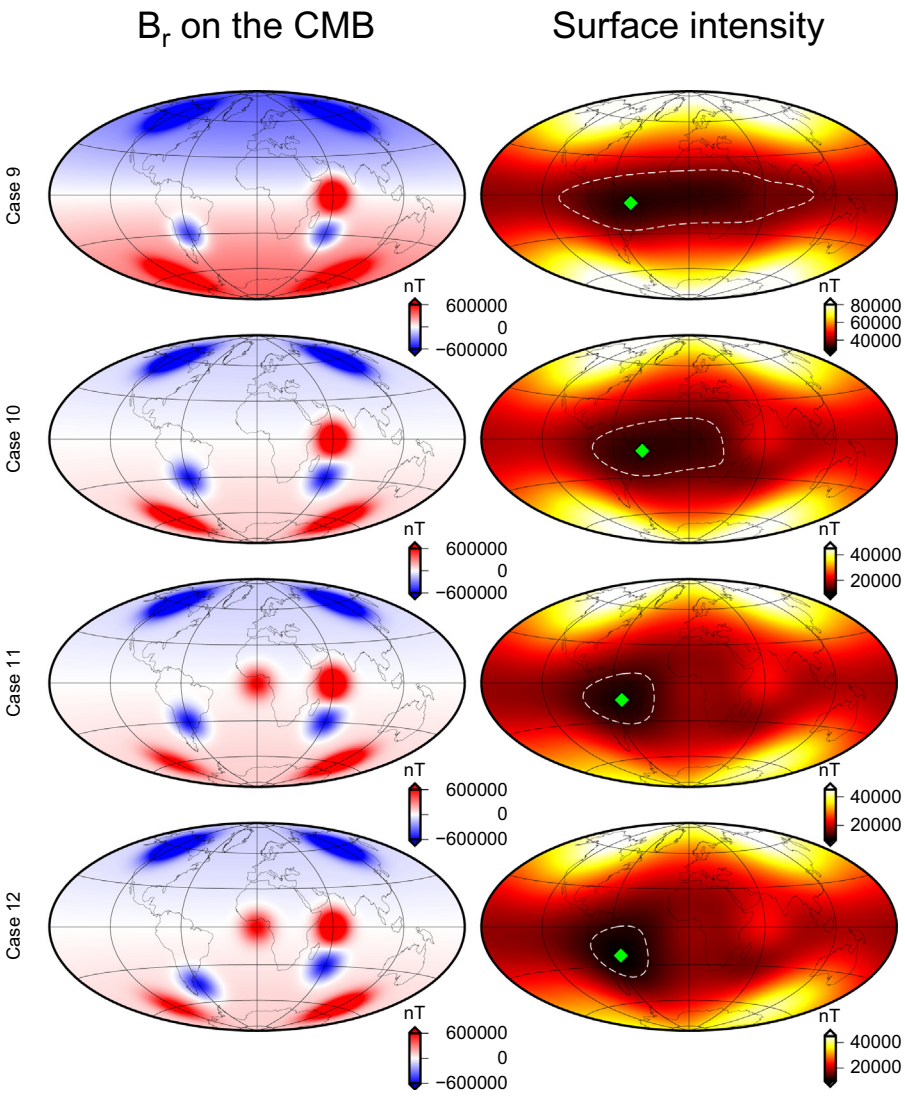

Fig. 3. As in Fig. 2 for cases 9, 10, 11 and 12 (see Table 1).

ing F_{min} longitude is determined by the other RFP. The latitude of the F_{min} is again close to the equator.

As mentioned above the level of axial dipolarity plays a role in the F_{min} latitude. With a purely axial dipolar field the F_{min} is exactly at the equator. In case 10 we therefore strongly reduced the background field, with otherwise the same patches configuration as in case 9. The background field reduction leads to an increase in the F_{min} latitude by 3°, but its longitude is less dictated by the South America RFP. In addition the F_{min} area $\mathcal{A}$ is larger, thus the F_{min} is shallower and hence less well defined (see Table 1).

In case 11 we added an NFP centered at the equator at longitude 0°, and we reduced the amplitude of the high-latitude NFP below south Pacific which has been decreasing in the historical era (Amit et al., 2011). The weaker high-latitude NFP below south Pacific increases the influence of the South America RFP resulting in F_{min} 4° farther away from the equator. The longitude is more dictated by the South America RFP than in cases 9–10 and is practically identical to that of the present-day geomagnetic field (Table 1). The new equatorial NFP is located right in between the longitudes of the two RFPs, hence its influence on the F_{min} longitude is minor.

In case 12 the RFP below South America was dislocated to the south closer to its position in the current geomagnetic field (Finlay et al., 2015). This resulted in a remarkable increase of 9° in the F_{min} latitude. Overall, case 12 gives an F_{min} location rather close to the SAA position in the CHAOS5 model at 2003 (see Table 1).

The m_z/m_z^D value decreases progressively from case 10 to 12, and consequently the F_{min} latitude also progressively increases. Likewise, the F_{min}/F_{min}^D value decreases from case 10 to 12 as the relative role of the RFPs increases. The area $\mathcal{A}$ is also progressively reduced, indicating increasing roughness of the field with more localized and better defined F_{min}.

3.3. Minimum surface intensity secular variation scenarios

Here we use synthetic models to investigate some possible future scenarios for the SAA. For this purpose we recall the radial component of the magnetic induction equation at the top of the core (where the radial velocity vanishes)

$$\frac{\partial B_r}{\partial t} = -\vec{u}_h \cdot \nabla B_r - B_r \nabla_h \cdot \vec{u}_h + \eta \left(\frac{1}{r_o^2} \frac{\partial^2}{\partial^2 r} (r^2 B_r) + \nabla_h B_r \right) \tag{11}$$

where B_r is the radial field, t is time, $\vec{u}_h$ is the tangential velocity vector, $\nabla_h = \nabla - \frac{\partial}{\partial r}$, η is the magnetic diffusivity, r_o is the core

radius and r is the radial coordinate. The term on the left hand side of (11) is the secular variation (SV). The terms on the right hand side of (11) represent magnetic advection, stretching and radial and tangential diffusion, respectively. We chose case 12 as an initial configuration, and then applied simple kinematic effects of advection (non-uniform westward drift), stretching (contraction/expansion with increased/decreased amplitude) and radial diffusion (intensification) of selected patches. These kinematic effects correspond to some simple solutions of (11).

First we considered the translation of low- and mid-latitude patches, while high-latitude NFPs are kept stationary. Westward drift is a prominent feature of the historical field (Bullard et al., 1950). However, the drift is not uniform. SV peaks appear at the equator and mid-latitudes of the Southern Hemisphere (Finlay and Jackson, 2003; Aubert et al., 2013). Core flow models also exhibit differential rotation with stronger zonal flows at low- and mid-latitudes of the Southern Hemisphere (Amit and Olson, 2006; Holme and Olsen, 2006). In contrast, it has been proposed that high-latitude NFPs are locked to lower mantle thermal anomalies (Gubbins et al., 2007; Willis et al., 2007). Although these NFPs do exhibit some mobility (Amit et al., 2011), the motion of lower latitude patches is faster and more monotonous.

We applied a classical westward drift rate of 0.2°/yr (Bullard et al., 1950) over a period of 100 yr to the low- and mid-latitude patches only. In longitude the F_{min} moves westward in a rather steady rate of 0.13°/yr (Fig. 4a). The F_{min} latitude remains practically unchanged. The slower westward motion of the F_{min} indicates an effect of the stationary NFPs. In particular, the presence of the NFP below South Pacific slows the F_{min} as it drifts towards this NFP.

RFPs emergence may be related to upwelling at the top of the core (Bloxham, 1986; Aubert et al., 2008), whereas NFPs may be concentrated by downwelling near the edge of the tangent cylinder (Olson et al., 1999; Peña et al., 2016). We produced such stretching effects by changing a patch width σ while compensating with an inverse change in its amplitude A_0. To conserve magnetic flux the width and amplitudes changes obey the relation (Roberts, 2007):

$$\frac{\sigma(t_0)}{\sigma(t_1)} = \frac{A_0(t_1)}{A_0(t_0)} \tag{12}$$

where t_0 and t_1 denote two snapshots of the synthetic field. We applied width changes to the RFP below South America which strongly affects the F_{min} location in case 12.

Fig. 4b shows that a wider South America RFP caused by local upwelling reduces the F_{min} latitude while the F_{min} longitude drifts eastward. This F_{min} motion indicates that as the South America RFP weakens it somewhat loses ground to the Africa RFP in terms of determining the F_{min} position. Note that the RFP expansion affects less the F_{min} longitude than its latitude. In addition a wider RFP reduces the field roughness leading to a less localized and less well defined F_{min}. When the RFP is contracted by downwelling the F_{min} position remains practically unchanged. This suggests that our choice of patches width is already rather concentrated and an asymptotic behavior is reached when further concentration is applied.

The detectability of diffusion in the observed geomagnetic SV is under debate. It has been demonstrated that field models can be constructed assuming frozen-flux (O'Brien et al., 1997; Jackson et al., 2007). In contrast, proliferation of RFPs, in particular below the Atlantic, has been proposed as a significant cause for the decrease of the geomagnetic dipole intensity (Gubbins, 1987; Olson and Amit, 2006; Finlay et al., 2012). Non-zero radial field integrals over regions bounded by null-flux curves provide evidence for flux expulsion (Gubbins and Bloxham, 1986; Chulliat and Olsen, 2010), though such calculations might be biased by imprecise topology of null-flux contours (Gillet et al., 2013). Core

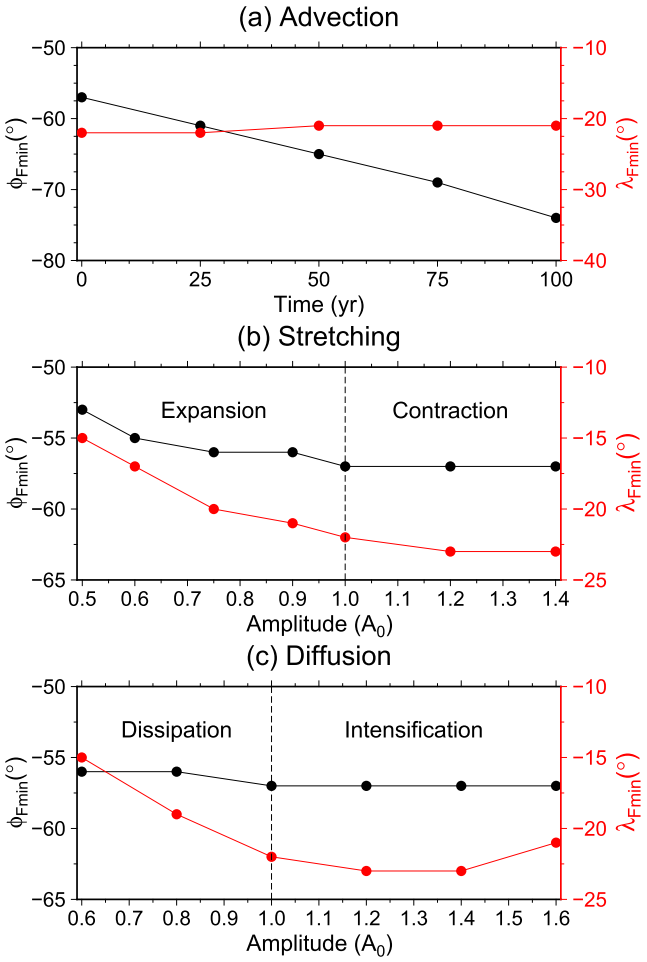

Fig. 4. Changes of F_{min} longitude ϕ_{Fmin} (black, left axis) and latitude λ_{Fmin} (red, right axis) due to (a) 0.2°/yr westward drift of low- and mid-latitude patches over 100 yr, (b) expansion/concentration of the South America RFP and (c) intensification/dissipation of the RFPs compensated by dissipation/intensification of Northern Hemisphere high-latitude NFPs, respectively. Case 12 (Table 1) is used as an initial field. Longitude and latitude are given in degrees. The vertical black dashed line in (b) separates expansion (left) and contraction (right) SV scenarios. The vertical black dashed line in (c) separates dissipation (left) and intensification (right) SV scenarios. (For interpretation of the references to colour in this figure legend, the reader is referred to the web version of this article.)

flow inversions from geomagnetic SV commonly neglect diffusion based on large magnetic Reynolds number estimates (Roberts and Scott, 1965). However, numerical dynamos models show clear radial diffusion SV contributions at the top of the shell even for Earth-like magnetic Reynolds numbers (Amit and Christensen, 2008; Finlay et al., 2016).

We applied amplitude changes to selected patches of case 12 while maintaining their width fixed, in order to mimic radial diffusion SV. The amplitude range considered here corresponds to the amplification range of the total reversed flux in the Southern Hemisphere over 100 yr (Olson and Amit, 2006). RFPs were intensified/dissipated while Northern Hemisphere high-latitude NFPs were dissipated/intensified, respectively, to compensate for the change in the total magnetic flux. The results in Fig. 4c show that the F_{min} longitude is practically constant for any RFPs amplitude. RFPs dissipation clearly reduces the F_{min} latitude due to an increasing axial dipole effect. RFPs intensification gives initially higher F_{min} latitude, but further intensification surprisingly reduces the F_{min} latitude.

Lastly, we explore the effects of the SV kinematic scenarios on the value of minimum intensity and its area $\mathcal{A}$ (Fig. 5). The effects

of westward drift, which were found to be proeminent in changing the F_{min} longitude (Fig. 4), are the least efficient in changing F_{min}/F^D_{min} and $\mathcal{A}$. The ratio F_{min}/F^D_{min} and the area $\mathcal{A}$ are reduced/increased by contraction/expansion due to stretching, respectively. Intensification/dissipation due to diffusion reduce/increase F_{min} and the area $\mathcal{A}$, respectively. Diffusion is by far the most efficient mechanism in terms of intensity change.

3.4. Summary

Our main findings from the synthetic tests are: (i) the longitude of the F_{min} is clearly dictated by RFPs; (ii) the F_{min} tends to be far away from the NFPs; (iii) the latitude of the F_{min} is affected by the competition between the axial dipole and the RFPs. Relatively strong axial dipole will result in low-latitude F_{min}, whereas relatively strong RFPs will give F_{min} closer to the latitude of the RFPs; (iv) NFPs may cause a reduction in the F_{min} latitude if located next to the RFP that determines the F_{min} longitude; (v) strong RFPs give more pronounced intensity minimum confined to a smaller area.

The examined SV scenarios provide some speculative predictions for the SAA: (i) westward drift of low- and mid-latitude patches will lead to SAA westward drift, though at a lower speed; (ii) South America RFP dispersion by upwelling will move the SAA to lower latitudes and to a lesser extent eastward; (iii) the influence of South America RFP contraction by downwelling on the SAA motion reaches an asymptote for highly concentrated patches; (iv) RFPs intensification or dissipation will not affect the longitude of the SAA; (v) RFPs expulsion is the most efficient mechanism to reduce minimum surface intensity and to increase the field roughness.

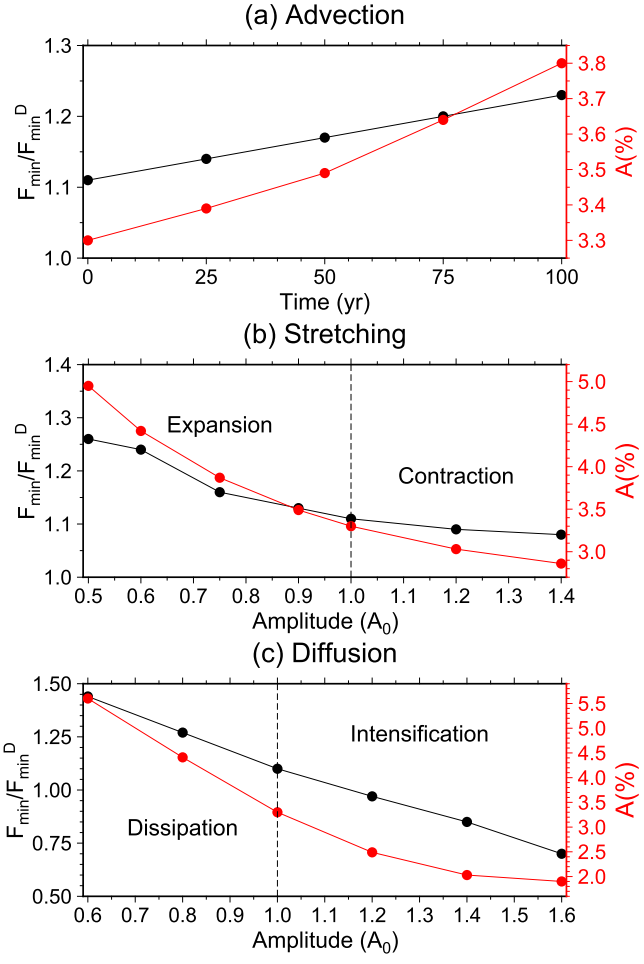

Fig. 5. As in Fig. 4 for changes of the ratio F_{min}/F^D_{min} (black, left axis) and the area $\mathcal{A}$ (red, right axis). Note the different scales. (For interpretation of the references to colour in this figure legend, the reader is referred to the web version of this article.)

4. Application to geomagnetic field models

We used the historical geomagnetic field model gufm1 (Jackson et al., 2000) for the period 1840–1990 and the field model CHAOS5 based on high quality global coverage satellite data (Finlay et al., 2015) for the period 1997–2015 to monitor the South Atlantic Anomaly (SAA). In addition we used the IGRF-12 model for the period 1980–2010 (Thébault et al., 2015) to fill the gap between gufm1 and CHAOS5. The gufm1 and CHAOS5 models were truncated at spherical harmonic degree $n_{max} = 14$. The IGRF-12 models were truncated at $n_{max} = 10$ and 13 before and from 2000, respectively. Obviously different regularizations were applied by the modelers depending on the data coverage and quality.

Fig. 6a shows the SAA minimum tracking over the historical and modern periods. Persistent westward drift is observed. A much slower poleward drift is also found. Between 1900 and 1940 the SAA minimum turned relatively more to the poleward direction. In the past 20 years the SAA minimum has been moving in a nearly purely westward direction. From 1840 to 2015, the SAA minimum has drifted from the mid Atlantic ($17°W$, $21°S$) to inland South Brazil ($53°W$, $28°S$), and its intensity has been gradually decreasing (see colors in Fig. 6a). The tracking for the IGRF-12 model connects well with those of the gufm1 and CHAOS5 models. The time evolution of the SAA minimum in longitude and latitude is also shown in Fig. 6. The longitude curve (Fig. 6b) shows roughly two trends, $\sim -0.38°/yr$ before and $\sim -0.16°/yr$ after 1900. The latitude curve (Fig. 6c) shows alternating faster/slower trends, with the latest transition of $\sim -0.054°/yr$ before and $\sim -0.004°/yr$ after 1950, clearly getting nearly constant in latitude at recent times. Overall between 1840 and 2015 the SAA minimum moved an angular distance of $\sim 33°$ from the South Atlantic to inland South Brazil.

Fig. 7a compares the time evolutions of the intensity of the SAA minimum and the absolute value of the axial dipole Gauss coefficient $|g^0_1|$. Although these two quantities are distinctive, both curves show approximately linear decreasing trends, with the SAA intensity decreasing much faster. The intensities of the SAA minimum and g^0_1 have been reduced by 25% and 9% respectively from 1840 to 2015. It is worth noting that the non-linear parts of the curves in Fig. 7a seem at some times out of phase. We removed the linear fits to these curves and then plotted the non-linear parts of the intensities of the SAA minimum and g^0_1 (Fig. 7b). The resulting two curves indeed have maxima/minima at different times, with a time-dependent delay. This delay is larger at earlier times than at recent times.

Fig. 8 shows five snapshots of the kernel functions centered at the time-dependent position of the SAA minimum (Fig. 6a). Because the SAA minimum changes its position with time, the geometric contribution of the radial field at the CMB to the surface field components also changes with time as reflected by the patterns of the kernel functions G_θ, G_ϕ and G_r. The radial kernel function G_r has the strongest values and accounts mostly for field structures in the region of the CMB right beneath the surface point. In the case of the SAA minimum, G_r is most sensitive to B_r at the CMB below mid Atlantic in 1850 to below inland south Brazil in 2010. The G_θ regions of sensitivity to B_r at the CMB are below the South Atlantic (negative values) and equatorial Atlantic (positive values) in 1850 to below Patagonia (negative values) and Amazon (positive values) in 2010. The G_ϕ sensitive regions to B_r at the CMB are below west South Africa (negative values) and east Brazil (positive values) in 1850 to below mid Atlantic (negative values) and west South America (positive values) in 2010. According to (8)

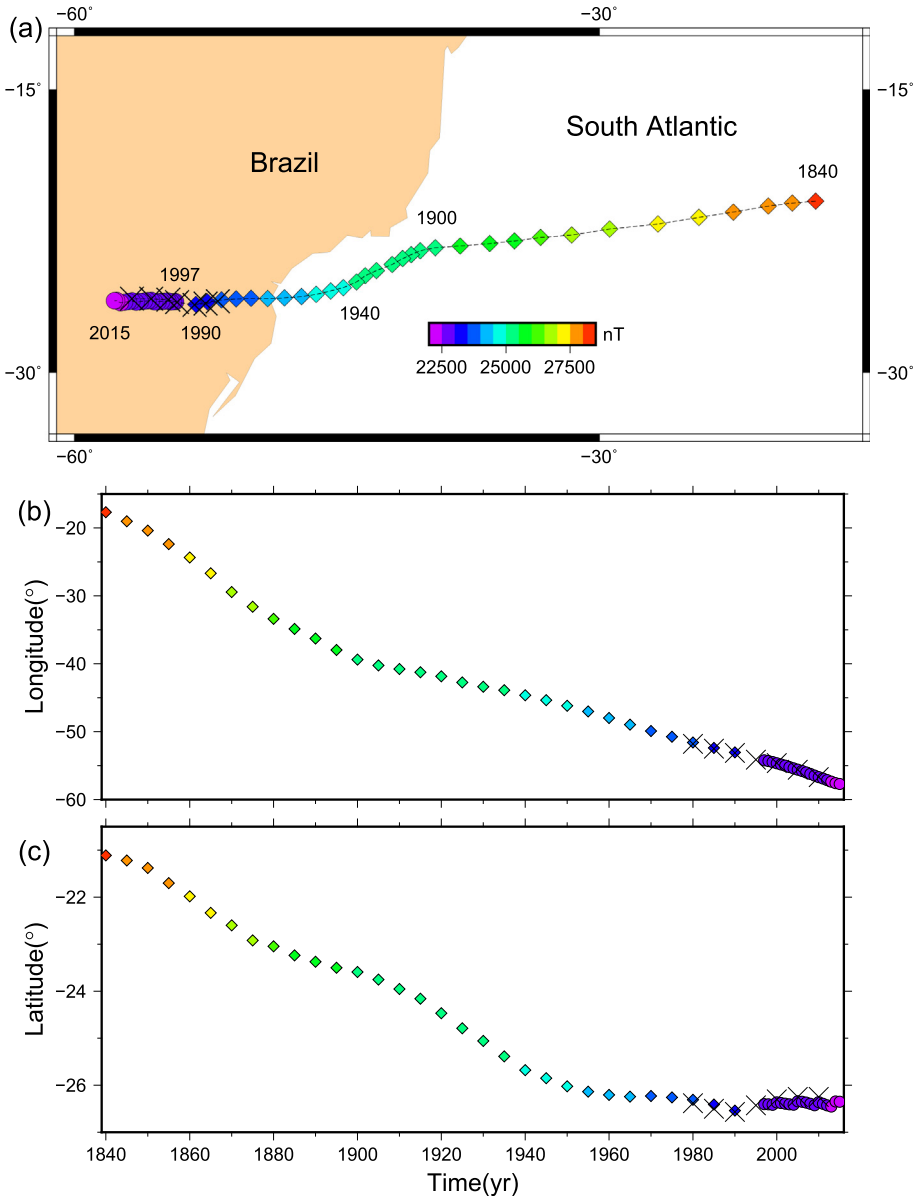

Fig. 6. Tracking of the South Atlantic Anomaly (SAA) minimum. Time-dependence of the SAA minimum at Earth's surface (a), in longitude (b) and latitude (c) based on the gufm1 (Jackson et al., 2000, diamonds), CHAOS5 (Finlay et al., 2015, circles) and IGRF-12 (Thébault et al., 2015, crosses) field models. Geomagnetic field intensities in nT are denoted by colors for gufm1 and CHAOS5.

G_θ, G_ϕ and G_r represent weights of the intensity kernel function G_F. The monopolar G_r and the positive surface B_r in the Southern Hemisphere give a monopolar positive contribution to G_F in the Southern Hemisphere. The bipolar G_θ and the negative surface B_θ give a bipolar contribution to G_F (negative/positive in the Northern/Southern hemisphere, respectively). The resulting G_F is the sum of these two dominant structures.

Corresponding snapshots of the surface field intensity, the intensity kernel function G_F with respect to the SAA minimum and the radial field B_r at the CMB with identified RFPs are shown in Fig. 9. In general, the SAA minimum is not found at the exact position of the G_F maximum. Moreover, at most snapshots the SAA is not found in the center of mass of the identified RFPs or the reversed flux region (Fig. 9). At 1850, the SAA minimum and the G_F maximum are close to two identified RFPs, but the SAA minimum is north of the G_F maximum and east of the RFPs. At 1890, a magnetic equator intrusion prevents RFPs identification (Terra-Nova et al., 2015). The SAA minimum is north of the intrusion and north of the G_F maximum. At 1930, 1970 and 2010, the SAA minimum and the G_F maximum are close to one RFP below Patagonia. However, both quantities are far from another RFP below Africa.

The distance between the SAA minimum and the G_F maximum is thus time-dependent. Fig. 10 shows this great-circle distance ΔD as a function of time. The SAA minimum is about $15^\circ \pm 3^\circ$ away from the G_F maximum. The ΔD value before 1880 exhibits a roughly constant trend oscillating between $\sim 15.5^\circ$ and $\sim 16.5^\circ$. In contrast, between 1885 and 1980 ΔD decreases monotonously from $\sim 17^\circ$ to $\sim 13^\circ$. ΔD has stable values of $12.1^\circ - 12.4^\circ$ from 1997 to 2015, although at two snapshots it deviates from this range. For the IGRF-12 model the ΔD value varies strongly between $\sim 12^\circ$ and $\sim 13.5^\circ$.

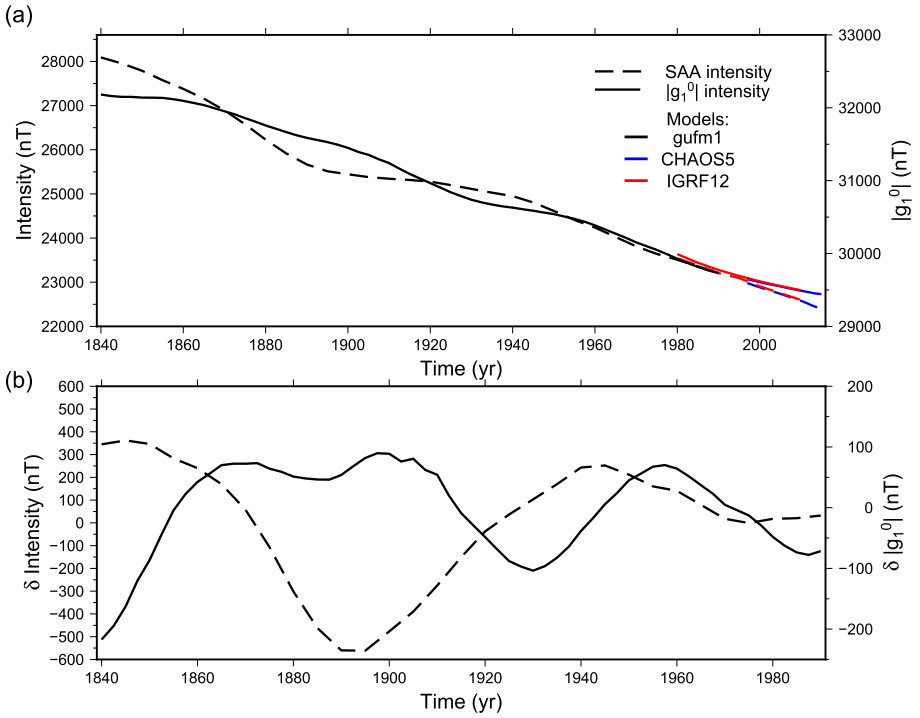

Fig. 7. (a): The time dependence of the intensity of the SAA minimum (dashed lines, left axis) and $|g_1^0|$ (solid lines, right axis) for the gufm1 (black), CHAOS5 (blue) and IGRF-12 (red) geomagnetic field models. (b): The non-linear part (δ) of the intensities of the SAA minimum (solid line) and g_1^0 (dashed line) for the gufm1 field model obtained by removing the respective linear fits from (a). Note the different scales on the right axes of (a) and (b). (For interpretation of the references to colour in this figure legend, the reader is referred to the web version of this article.)

In Fig. 10 we also plot the ratio between the powers of the axial dipole (AD) and the non-axial dipole (NAD) fields (e.g. Christensen et al., 2010):

$$AD/NAD = \frac{2(g_1^0)^2}{2((g_1^1)^2 + (h_1^1)^2) + \sum_{n=2}^{n_{max}} \left((n+1)\left(\frac{a}{c}\right)^{2n-2} \sum_{m=0}^{n} (g_n^m)^2 + (h_n^m)^2 \right)} \quad (13)$$

where n is degree, m is order, and the sets g_n^m and h_n^m are the Gauss coefficients. The truncation degree n_{max} affects the absolute values of (13), but its temporal trend is less affected by n_{max} (compare Fig. 10 with Fig. 1 of Christensen et al. (2010)). The AD/NAD ratio and ΔD are correlated after 1885 (see Fig. 10). Prior to 1885 reversed flux regions are less prominent thus the location of the SAA minimum is more uncertain, as evident in the oscillating behavior of ΔD at that time. Later the relative NAD power rapidly increases, more RFPs appear and consequently the SAA minimum becomes more robust in terms of its relation to the field morphology at the CMB. The two quantities display similar trends even with the fall in the AD/NAD ratio for the CHAOS5 model due to its increased spatial resolution (Finlay et al., 2015). The correlation between ΔD and AD/NAD after 1885 observed in gufm1 and CHAOS5 is not found in IGRF-12. It is worth noting that IGRF-12 is the mean of several independent candidate field models (Thébault et al., 2015) and as such it is considered somewhat less robust, in particular prior to 2000.

Next, we compare the positions of RFPs at the CMB with the position of the SAA minimum at the surface (Fig. 11). In longitude, the SAA minimum is close to RFPs in the Southern Atlantic before 1860. The SAA minimum cannot be related to RFPs between 1860 and 1900 due to a magnetic equator intrusion in this period (see snapshot 1890 in Fig. 9) that prevents RFPs identification (Terra-Nova et al., 2015). After 1900, the SAA minimum exhibits westward drift similar to the Patagonia RFP (Terra-Nova et al., 2015). However, additional RFPs appear close to Africa, also exhibiting westward drift, especially after 1997. In latitude, both the SAA minimum and the Patagonia RFP move poleward whereas the Africa RFP moves equatorward. Note that the latitudes of the SAA minimum and the RFPs become nearly constant with time.

Why is the SAA minimum close to the Patagonia RFP but far from the Africa RFPs? Why do the SAA minimum and the RFPs latitudes become nearly constant with time? To address these questions we calculated the integrated normal flux in the Southern Hemisphere (i.e. $B_r > 0$) at the CMB $< B_r^N(\phi) >$ vs. longitude:

$$< B_r^N(\phi) > = \frac{2}{\pi} \int_{\frac{\pi}{2}}^{\pi} B_r(\phi, \theta) sin\theta \mathrm{d}\theta \quad (14)$$

Fig. 12 shows five snapshots of $< B_r^N(\phi) >$. The two high-latitude normal flux patches (NFPs) are evident by the two peaks between 90° W and 130° W and between 80° E and 120° E. The former is weaker and loses strength with time, as reported by Amit et al. (2011). The peak between 10° E and 60° E that intensifies with time and drifts westward corresponds to a low-latitude NFP (see Fig. 9) below Africa (Jackson, 2003). We argue that the presence of this intense NFP at low latitudes causes the SAA minimum to be away from Africa. In contrast, no intense low-latitude NFP is observed around South America (Figs. 9 and 12). Following the insights gained from the synthetic tests (see e.g. synthetic cases 8–12 in Figs. 2, 3 and Table 1), this may suggest that the longitude of the SAA minimum is determined by the Patagonia RFP. Likewise, the southwestward migration of the SAA minimum is possibly determined by the motion of the Patagonia RFP. Indeed the westward drift of the SAA minimum correlates with the westward drift of the Patagonia RFP. The poleward drift of the SAA minimum is probably associated to both the weakening of the high-latitude

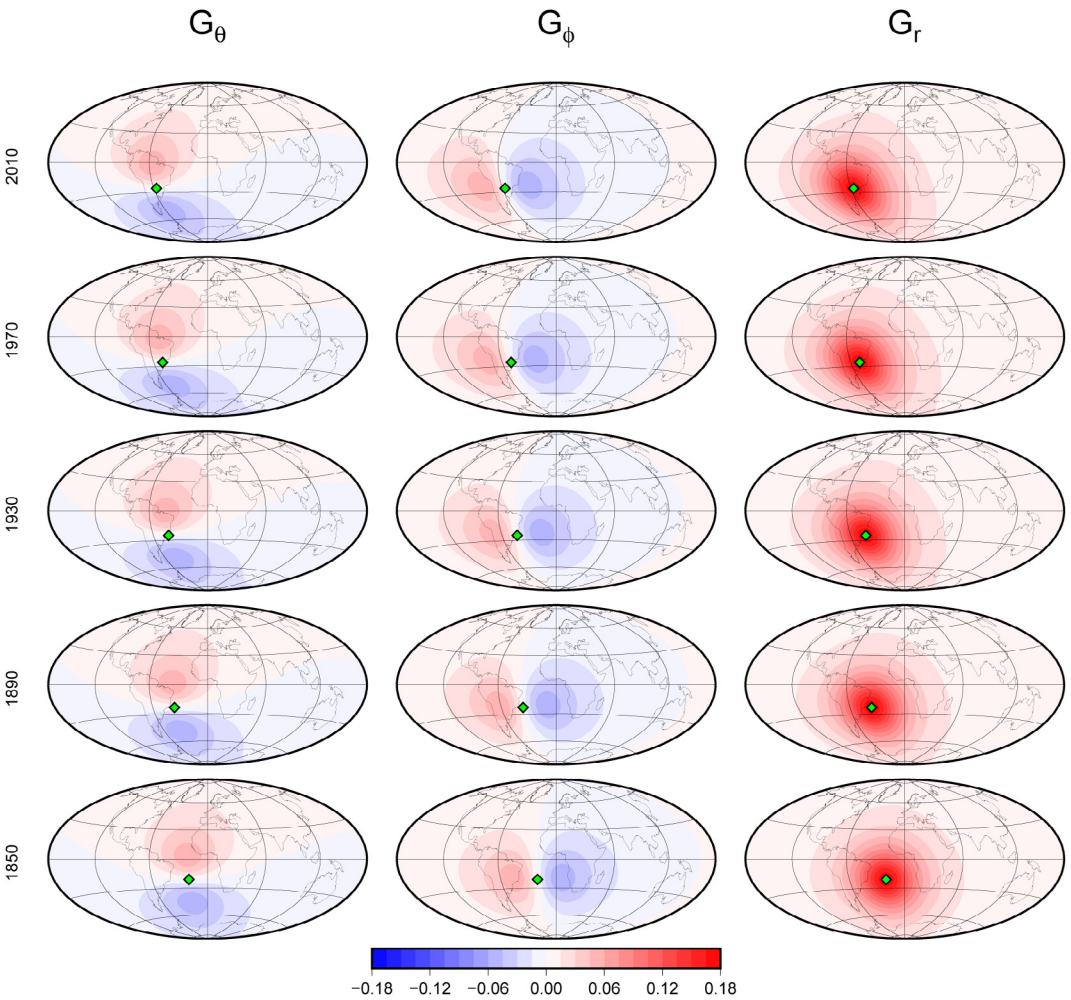

Fig. 8. Kernels G_θ, G_ϕ and G_r for the tracked positions of the SAA minimum in Fig. 6 in the years 1850, 1890, 1930, 1970 (gufm1) and 2010 (CHAOS5). The SAA minimum is denoted by green diamonds. (For interpretation of the references to colour in this figure legend, the reader is referred to the web version of this article.)

NFP below South Pacific (Fig. 12) as well as the migration of the Patagonia RFP poleward (see Fig. 11), both of which reduce the ADM.

5. Discussion

The intensity of the SAA minimum has been decreasing much faster than the g_1^0 intensity since 1840 (Fig. 7a). Thus the collapse of $|g_1^0|$ is not enough to explain the weakening in the SAA intensity and an intensification of non-dipolar field structures must be invoked (e.g. Hartmann and Pacca, 2009). The non-linear parts of the intensities of the SAA minimum and g_1^0 (Fig. 7b) are shifted, with this delay being larger for the earlier period and smaller more recently.

The morphology of G_F shows that the SAA minimum is mostly sensitive to field structures beneath it (Fig. 9). However, there are considerable differences between the positions of the SAA minimum and the G_F maximum. We showed that these differences are related to the relative axial dipolarity of the field (Fig. 10). In a hypothetical pure axial dipole field configuration the minimum surface intensity would be located along the entire geographic equator. Additional non-axial dipole field contributions lead to more complex morphologies resulting in a localized surface intensity minimum. Weaker axial dipole therefore gives more robust and stable minimum intensity surface point with more localized influence of the CMB field just below it.

The synthetic tests shed light on the relation between magnetic flux patches at the CMB and the intensity at the Earth's surface. These tests clearly demonstrate that RFPs prescribe the longitude of the minimum intensity at the surface. The latitude of F_{min} is a consequence of the competition between the latitude of the RFPs and the axial dipolarity of the field. If the axial dipole is strong the minimum intensity point is located closer to the equator, whereas if the RFPs are strong F_{min} appears at latitudes closer to the RFPs. The synthetic field model with the closest F_{min} coordinates to those of the SAA in CHAOS5 has a weaker high-latitude NFP below South Pacific and the RFP below South America is at higher latitudes than the Africa RFP, in agreement with the present geomagnetic field (as in e.g. Finlay et al., 2015). This SAA recovery demonstrates that indeed the interplay among the most intense patches determines the SAA position while the impact of weaker smaller-scale patches is likely secondary.

Starting from a synthetic field model with surface intensity minimum location close to the SAA, we explored F_{min} path predictions based on some simple SV scenarios (Fig. 4). Westward drift of low- and mid-latitude patches move F_{min} westward, but at a rate about 2/3 slower. Expansion of the South America RFP moves F_{min} equatorward and slightly eastward whereas its contraction may give some westward drift if the concentration is not yet at the asymptote. Intensification of the Southern Hemisphere RFPs

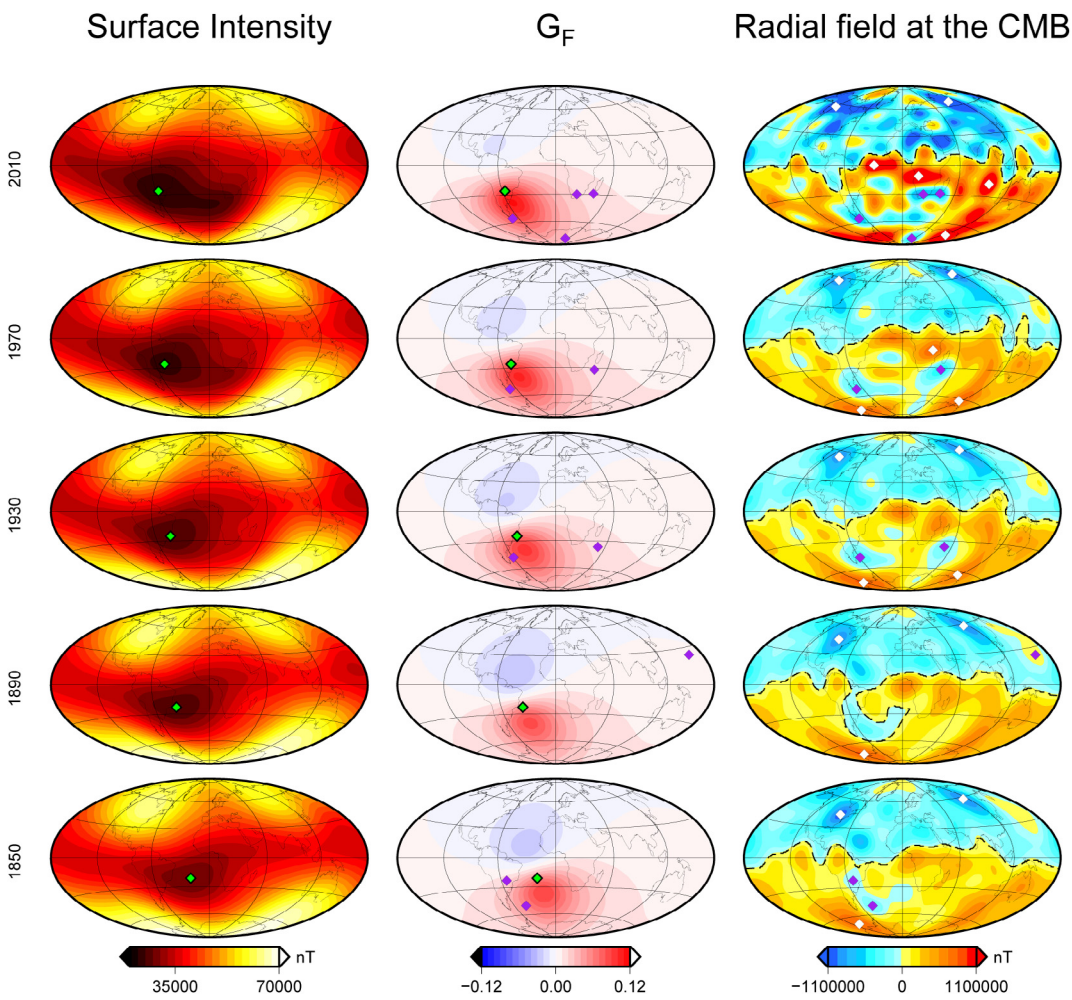

Fig. 9. Field intensity at Earth's surface (left), intensity kernel G_F (middle) and radial field at the CMB (right) for 1850, 1890, 1930, 1970 (gufm1) and 2010 (CHAOS5). The SAA minimum is denoted by green diamonds (left and middle) and the identified reversed flux patches (RFPs) and normal flux patches (NFPs) are denoted by purple diamonds (middle and right) and white diamonds (right), respectively. Dashed lines denote the identified magnetic equator (right). Both CMB and surface fields are in nT. (For interpretation of the references to colour in this figure legend, the reader is referred to the web version of this article.)

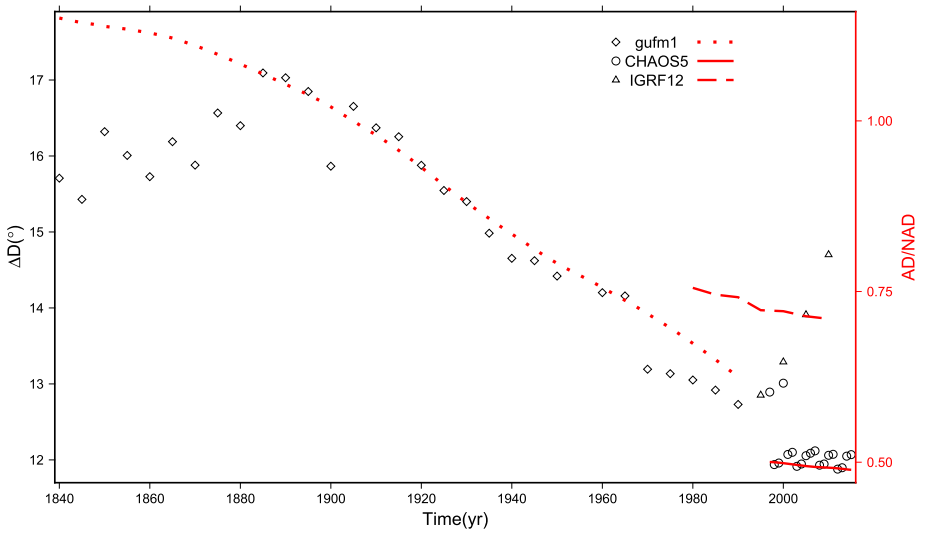

Fig. 10. Time-dependence of the great-circle distance ΔD between the SAA minimum and the G_F maximum (left axis), and of the ratio of axial dipole power to non-axial dipole power AD/NAD (right axis). ΔD is denoted by diamonds, circles and triangles for the gufm1, CHAOS5 and IGRF-12 field models, respectively. A few points (three in IGRF-12 and one in gufm1) have values that are out of range. The ratio AD/NAD is denoted by dotted, solid and dashed red lines for gufm1, CHAOS5 and IGRF-12, respectively. (For interpretation of the references to colour in this figure legend, the reader is referred to the web version of this article.)

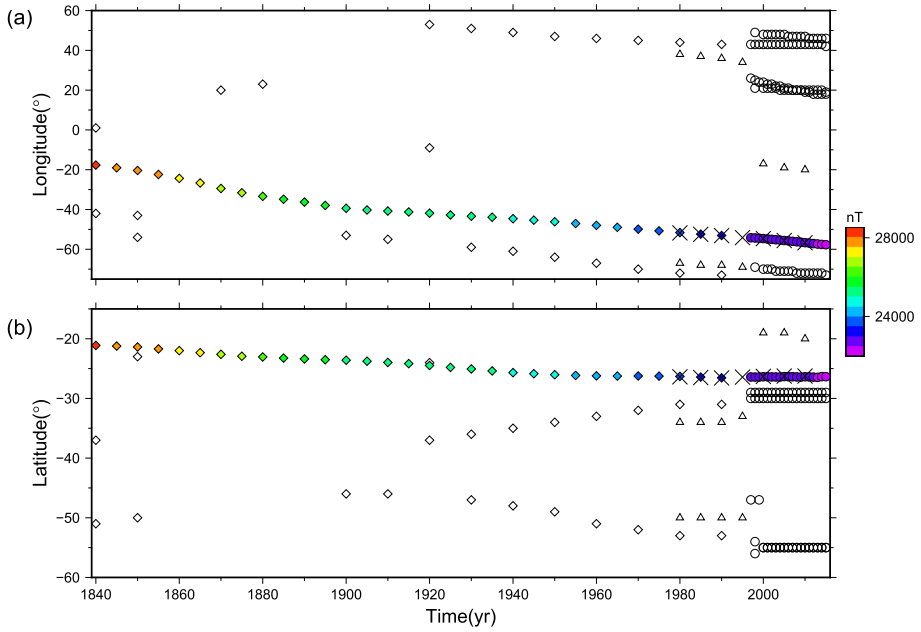

Fig. 11. As in Fig. 6b and c including identified reversed flux patches (RFPs). The RFPs are denoted by non-filled diamonds, circles and triangles for the gufm1, CHAOS5 and IGRF-12 field models, respectively. A few RFPs (located in the Northern Hemisphere or/and further east of Africa in gufm1 and CHAOS5 field models and only in the Northern Hemisphere for the IGRF-12 field model) have values out of range.

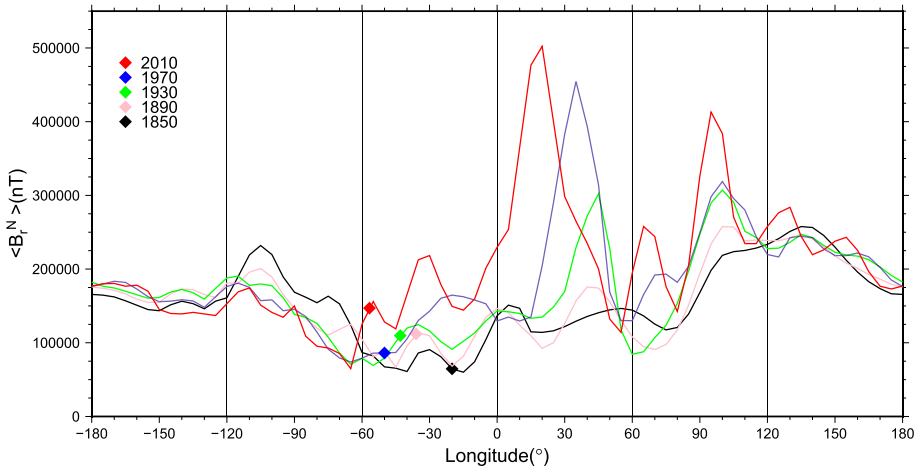

Fig. 12. Integrated normal flux $< B_r^N >$ at the core-mantle boundary calculated over the Southern Hemisphere vs. longitude. Each colored line denotes another snapshot (see legend). Diamonds denote the longitudes of the SAA minimum. (For interpretation of the references to colour in this figure legend, the reader is referred to the web version of this article.)

by radial diffusion does not affect the F_{min} longitude. In contrast, intensification of RFPs due to radial diffusion is the most efficient mechanism to reduce the intensity of the surface field minimum (Fig. 5). We conclude that while the SAA trajectory can be explained by a frozen-flux SV, the decrease in its intensity requires the presence of radial diffusion SV.

Our analysis of geomagnetic field models highlights the different roles of specific RFPs and NFPs in the localization of the SAA minimum. Before 1900 the SAA minimum was close to the center of mass of the reversed flux region in the Southern Hemisphere (see Fig. 9). However, at more recent times, the SAA minimum moved farther from this center of mass towards the longitude of an identified RFP below Patagonia. We argue that the reason for this SAA minimum location is that the intense low-latitude NFPs cause the SAA minimum to be away from the Africa RFPs, while low-latitude NFPs are absent below South America (as in synthetic cases 9–12). In addition, the South Pacific high-latitude NFP causes the SAA minimum to reside north of the Patagonia RFP (as in synthetic cases 4 and 5). The geomagnetic field models indicate a prominent westward drift as well as some poleward drift of the SAA minimum (Fig. 6). Comparable westward drift is observed for the Patagonia RFP (Terra-Nova et al., 2015). The poleward drifts of the Patagonia RFP and the SAA minimum are also similar. In addition, the poleward drift of the SAA minimum is also influenced by the weakening of the South Pacific NFP at high latitudes (Amit et al., 2011).

The westward drift of the SAA minimum is time-dependent (Fig. 6b). Prior to 1900 the SAA drifted westward relatively fast whereas after 1900 the drift was more than twice slower. Poleward drift shows alternating faster/slower trends: recently, prior to 1950 the SAA moved poleward relatively fast whereas after 1950 the poleward drift significantly diminished. The westward drift of the

SAA minimum may have decelerated because of the emergence of the Africa RFP at 1920 (Figs. 9 and 11). The poleward deceleration of the SAA minimum may have occurred due to the poleward deceleration of the Patagonia RFP (Fig. 11) and the decrease in the rate of intensity drop of the high-latitude NFP below South Pacific with time (see Fig. 12).

The rate of westward drift of geomagnetic CMB flux patches (Finlay and Jackson, 2003; Aubert et al., 2013) is comparable to the recent SAA westward drift in Fig. 6b. This is in contrast to our synthetic advective SV scenario in which the SAA drifts at a rate of $\sim 2/3$ of the patches drift rate (Fig. 4a). One possible explanation is uniform drift over all latitudes, but this is in contradiction to most core flow models (Holme, 2015). Another possibility is a combined advection and stretching SV, but RFP expansion actually gives eastward drift (Fig. 4b). Radial diffusion has a minor impact on the SAA longitude (Fig. 4c). The historical SAA drift rate was probably caused by a somewhat more complex SV scenario involving several prominent patches as suggested in our analysis of the geomagnetic field.

Aubert (2015) performed a forecast of the SAA minimum until 2115 predicting a faster SAA westward drift than in recent times and slight northward drift. Such faster SAA westward drift may arise due to faster westward drifting low- and mid-latitude patches, further weakening of the NFP below south Pacific and intensification of the low-latitude NFP below Africa. The predicted northward SAA drift by Aubert (2015) could originate from RFP expansion by stretching effects (Fig. 4b).

We argue that the SAA minimum is indeed related to RFPs, but also to the positions of low- and high-latitude NFPs, as we demonstrated in the synthetic tests. A persistent extension of a reversed flux region coupled with an NFP at one border would cause the SAA minimum to drift away from the center of reversed flux possibly causing the westward drift of the SAA minimum. If the axial dipole eventually increases due to shrinking of the reversed flux region below the South Atlantic, the surface minimum may lose its robustness and appear at sporadic longitudes near the magnetic equator.

Maps of advective sources of ADM changes (Olson and Amit, 2006; Finlay et al., 2016) showed that below Asia equatorward advection of an NFP decreases the ADM while below North America poleward drift of an NFP increases the ADM. The opposite motions of these two Northern Hemisphere NFPs cancel out their contributions to ADM changes. Below the Indian Ocean the equatorward drift of an NFP decreases the ADM, while below South America no significant advective ADM source is observed. Thus, the Patagonia RFP breaks the symmetry of ADM changes and is responsible to the decrease of the ADM. Our results show that the same field structure, the Patagonia RFP, is also the geomagnetic feature at the CMB that mostly determines the location and mobility of the SAA minimum.

Several archeointensity studies based on archeological materials from Africa and South America claimed that the geomagnetic field variations in these regions are attributed to the SAA time evolution (e.g. Hartmann et al., 2010, 2011; Goguitchaichvili et al., 2011, 2012, 2015; Roperch et al., 2014, 2015; Osete et al., 2015; Tarduno et al., 2015; Poletti et al., 2016; Shah et al., 2016). Tarduno et al. (2015) argued for persistent low field intensity associated to the SAA. They hypothesized that the SAA influences the magnetic field in Africa as early as ~1200. Aubert (2015) predicted continued SAA westward drift until reaching eastern Pacific Ocean at 2115. According to these two studies there is ~1000 yr of minimum field intensity in the Southern Hemisphere, possibly from Africa to eastern Pacific Ocean. Tarduno et al. (2015) also proposed that topographic heterogeneities in the lowermost mantle at the edge of a low shear wave velocity province located below Africa are responsible for the emergence of RFPs at the CMB and the low intensity antique field there. Terra-Nova et al. (2016) used various archeomagnetic field models to show that RFPs have statistically preferred positions, and that these positions may be prescribed by heat flux heterogeneities in the lowermost mantle. If the SAA minimum has indeed preferred positions its current westward drift must cease at some point.

In summary, combining the tracking of the SAA minimum at Earth's surface, the identification of RFPs at the CMB, the use of kernels and accounting for NFPs at the CMB, we investigated the relation between CMB geomagnetic flux patches and the SAA minimum. We showed that the level of axial dipolarity of the field determines the stability of the relation between the SAA and RFPs. The position and motion of the SAA minimum are highly influenced by the interplay among several robust geomagnetic flux patches at the CMB: an RFP below Patagonia, the South Pacific high-latitude NFP and the low-latitude intense NFPs near Africa. Simple SV scenarios applied to a synthetic field model with some realistic features allowed to speculate possible future paths of the SAA.

New geomagnetic measurements may improve the identification and tracking of RFPs and SAA at present, in particular at South America. Overall, further monitoring of the surface intensity of the geomagnetic field and its morphology at the CMB by ground observatories and dedicated satellites (e.g. the currently orbiting Swarm mission) as well as reliable archeomagnetic data from Africa and South America for periods before the observatories era will shed light on the relation between the SAA minimum and kinematic processes originating in the outer core.

Acknowledgements

We are grateful to Phil Livermore and an anonymous reviewer for their constructive comments that improved the manuscript. The Gauss coefficients of the gufm1, CHAOS5 and IGRF-12 field models used in this paper are available respectively at http://jupiter.ethz.ch/cfinlay/gufm1.html, http://www.spacecenter.dk/files/magnetic-models/CHAOS-5/ and http://www.ngdc.noaa.gov/IAGA/vmod/igrf12coeffs.txt. F. T-N. acknowledges The National Council for Scientific and Technological Development (CNPq/Brazil) for grant 206997/2014-0. F. T-N., H. A. and K. J. P. were partly supported by the Centre National des Études Spatiales (CNES). G. A. H. thanks CAPES (grant AUXPE 2043/2014) and CNPq/Brazil (grant 454609/2014-0). R. I. F. T. is supported by CNPq/Brazil PQ (grant 304934/2014-3). K. J. P. is also supported by Région Pays de la Loire and FAPERJ (grant E-26/2002.803/2015). This work acknowledges the financial support from Région Pays de la Loire, project GeoPlaNet (convention N° 2016-10982).

References

Amit, H., 2014. Can downwelling at the top of the Earth's core be detected in the geomagnetic secular variation? Phys. Earth Planet. Inter. 229, 110–121.
Amit, H., Christensen, U.R., 2008. Accounting for magnetic diffusion in core flow inversions from geomagnetic secular variation. Geophys. J. Int. 175, 913–924.
Amit, H., Korte, M., Aubert, J., Constable, C.G., Hulot, G., 2011. The time-dependence of intense archeomagnetic flux patches. J. Geophys. Res. 116, B12106. http://dx.doi.org/10.1029/2011JB008538.
Amit, H., Olson, P., 2006. Time-average and time-dependent parts of core flow. Phys. Earth Planet. Inter. 155, 120–139.
Aubert, J., 2015. Geomagnetic forecasts driven by thermal wind dynamics in the Earth's core. Geophys. J. Int 203, 1738–1751.
Aubert, J., Aurnou, J., Wicht, J., 2008. The magnetic structure of convection-driven numerical dynamos. Geophys. J. Int. 172, 945–956.
Aubert, J., Finlay, C.C., Fournier, F., 2013. Bottom-up control of geomagnetic secular variation by the Earth's inner core. Nature 502, 219–223. http://dx.doi.org/10.1038/nature12574.
Bloxham, J., 1986. The expulsion of magnetic flux from the Earth's core. Geophys. J. R. Astr. Soc. 87, 669–678.
Bullard, E.C., Freedman, C., Gellman, H., Nixon, J., 1950. The westward drift of the Earth's magnetic field. Philo. Trans. R. Soc. London Ser. A 243, 67–92.

Christensen, U.R., Aubert, J., Hulot, G., 2010. Conditions for Earth-like geodynamo models. Earth Planet. Sci. Lett. 296, 487–496.
Chulliat, A., Hulot, G., Newitt, L.R., 2010. Magnetic flux expulsion from the core as a possible cause of the unusually large acceleration of the North magnetic pole during the 1990s. J. Geophys. Res. 115, B07101. http://dx.doi.org/10.1029/2009JB007143.
Chulliat, A., Olsen, N., 2010. Observation of magnetic diffusion in the Earth's outer core from Magsat, Orsted and CHAMP data. J. Geophys. Res. 115. http://dx.doi.org/10.1029/2009JB006994.
Constable, C., 2007a. Centennial- to millennial-scale geomagnetic field variations. In: Kono, M. (Ed.), Treatise on Geophysics, vol. 5. Elsevier Sci., New York, pp. 337–372.
Constable, C., 2007b. Non-dipole field. In: Gubbins, D., Herrero-Bervera, E. (Eds.), Encyclopedia of Geomagnetism and Paleomagnetism. Springer, Dordrecht, pp. 701–704.
Constable, C.G., Parker, R.L., Stark, P.B., 1993. Geomagnetic field models incorporating frozen-flux constraints. Geophys. J. Int. 113 (2), 419–433.
Finlay, C.C., 2008. Historical variation of the geomagnetic axial dipole. Phys. Earth Planet. Inter. 170, 1–14.
Finlay, C.C., Aubert, J., Gillet, N., 2016. Gyre-driven decay of the Earth's magnetic dipole. Nat. Commun. 7, 10422. http://dx.doi.org/10.1038/ncomms10422.
Finlay, C.C., Jackson, A., 2003. Equatorially dominated magnetic field change at the surface of Earth's core. Science 300, 2084–2086.
Finlay, C.C., Jackson, A., Gillet, N., Olsen, N., 2012. Core surface magnetic field evolution 2000–2010. Geophys. J. Int. 189, 761–781. http://dx.doi.org/10.1111/j.1365-246X.2012.05395.x.
Finlay, C.C., Maus, S., Beggan, C., Bondar, T., Chambodut, A., Chernova, T., Chulliat, A., Golovkov, V., Hamilton, B., Hamoudi, M., Holme, R., Hulot, G., Kuang, W., Langlais, B., Lesur, V., Lowes, F., Lhr, H., Macmillan, S., Mandea, M., McLean, S., Manoj, C., Menvielle, M., Michaelis, I., Olsen, N., Rauberg, J., Rother, M., Sabaka, T., Tangborn, A., Tffner-Clausen, L., Thbault, E., Thomson, A.W.P., Wardinski, I., Wei, Z., Zvereva, T.I., 2010. International geomagnetic reference field: the eleventh generation. Geophys. J. Int. 183, 1216–1230.
Finlay, C.C., Olsen, N., Tøffner-Clausen, L., 2015. DTU candidate field models for IGRF-12 and the CHAOS-5 geomagnetic field model. Earth Planets Space 67, 114.
Gillet, N., Jault, D., Finlay, C., Olsen, N., 2013. Stochastic modeling of the Earth's magnetic field: inversion for covariances over the observatory era. Geochem. Geophys. Geosyst. 14 (4), 766–786.
Goguitchaichvili, A., Greco, C., Morales, J., 2011. Geomagnetic field intensity behavior in South America between 400 ad and 1800 ad: first archeointensity results from Argentina. Phys. Earth Planet. Inter. 186, 191–197.
Goguitchaichvili, A., Loponte, D., Morales, J., Acosta, A., 2012. The archaeointensity of the Earth's magnetic field retrieved from Pampean ceramics (South America). Archaeometry 54 (2), 388–400.
Goguitchaichvili, A., Morales, J., Schavelzon, D., Vásquez, C., Gogorza, C., Loponte, D., Rapalini, A., 2015. Variations of the Earth's magnetic field strength in South America during the last two millennia: new results from historical buildings of Buenos Aires and re-evaluation of regional data. Phys. Earth Planet. Inter. 245, 15–25.
Gubbins, D., 1987. Mechanism for geomagnetic polarity reversals. Nature 326, 167–169.
Gubbins, D., 2004. Time Series Analysis and Inverse Theory for Geophysicists. Cambridge University Press, Cambridge, UK.
Gubbins, D., Bloxham, J., 1986. Geomagnetic field analysis IV – testing the frozen-flux hypothesis. Geophys. J. R. Astr. Soc. 84, 139–152.
Gubbins, D., Roberts, N., 1983. Use of the frozen-flux approximation in the interpretation of archaeomagnetic and paleomagnetic data. Geophys. J. R. Astr. Soc. 73, 675–687.
Gubbins, D., Willis, P.W., Sreenivasan, B., 2007. Correlation of Earth's magnetic field with lower mantle thermal and seismic structure. Phys. Earth Planet. Inter. 162, 256–260.
Hartmann, G.A., Genevey, A., Gallet, Y., Trindade, R.I.F., Etchevarne, C., Le Goff, M., Afonso, M.C., 2010. Archeointensity in Northeast Brazil over the past five centuries. Earth Planet. Sci. Lett. 296, 340–352.
Hartmann, G.A., Genevey, A., Gallet, Y., Trindade, R.I.F., Le Goff, M., Najjar, R., Etchevarne, C., Afonso, M.C., 2011. New historical archeointensity data from Brazil: evidence for a large regional non-dipole field contribution over the past few centuries. Earth Planet. Sci. Lett. 306, 66–76. http://dx.doi.org/10.1016/j.epsl.2011.03.030.
Hartmann, G.A., Pacca, I., 2009. Time evolution of the south atlantic magnetic anomaly. An. Acad. Bras. Cien. 81, 243–255.
Holme, R., 2015. Large-scale flow in the core. In: Olson, P. (Ed.), Treatise on Geophysics. . Second ed., vol. 8 Elsevier.
Holme, R., Olsen, N., 2006. Core surface flow modelling from high-resolution secular variation. Geophys. J. Int. 166, 518–528.
Hulot, G., Eymin, C., Langlais, B., Mandea, M., Olsen, N., 2002. Small-scale structure of the geodynamo inferred from Oersted and Magsat satellite data. Nature 416, 620–623.
Jackson, A., 2003. Intense equatorial flux spots on the surface of the Earth's core. Nature 424, 760–763.
Jackson, A., Constable, C.G., Walker, M.R., Parker, R.L., 2007. Models of Earth's main magnetic field incorporating flux and radial vorticity constraints. Geophys. J. Int. 171, 133–147. http://dx.doi.org/10.1111/j.1365-246X.2007.03526.x.
Jackson, A., Jonkers, A.R.T., Walker, M.R., 2000. Four centuries of geomagnetic secular variation from historical records. Philos. Trans. R. Soc. Lond. A358, 957–990.
Johnson, C.L., Constable, C.G., 1997. The time-averaged geomagnetic field: global and regional biases for 0–5 ma. Geophys. J. Int. 131, 643–666.
Kelly, P., Gubbins, D., 1997. The geomagnetic field over the past 5 million years. Geophys. J. Int. 128, 315–330.
Mikhlin, S.G., 1970. In: Mathematical Physics. An Advanced Course. North-Holland, London.
O'Brien, M.S., Constable, C.G., Parker, R.L., 1997. Frozen-flux modelling for ephocs 1915 and 1980. Geophys. J. Int. 171, 434–450.
Olson, P., Amit, H., 2006. Changes in earth's dipole. Naturwissenschaften 93, 519–542.
Olson, P., Christensen, U.R., Glatzmaier, G.A., 1999. Numerical modeling of the geodynamo: mechanisms of field generation and equilibration. J. Geophys. Res. 104, 10383–110404.
Osete, M., Catanzariti, G., Chauvin, A., Pavn-Carrasco, J., Roperch, P., Fernndez, V., 2015. First archaeomagnetic field intensity data from Ethiopia, Africa (1615 ± 12 AD). Phys. Earth Planet. Inter. 242, 24–35.
Pavón-Carrasco, F.J., De Santis, A., 2016. The South Atlantic Anomaly: the key for a possible geomagnetic reversal. Front. Earth Sci. 4, 40.
Peña, D., Amit, H., Pinheiro, K.J., 2016. Magnetic field stretching at the top of the shell of numerical dynamos. Earth Planets Space 38, 48.
Poletti, W., Trindade, R.I.F., Hartmann, G.A., Damiani, N., Rech, R.M., 2016. Archeomagnetism of Jesuit Missions in South Brazil (1657–1706 AD) and assessment of the South American database. Earth Planet. Sci. Lett. 445. 63-47.
Roberts, P.H., 2007. Theory of the geodynamo. In: Olson, P. (Ed.), Treatise on Geophysics, vol. 8. Elsevier Science.
Roberts, P.H., Scott, S., 1965. On analysis of the secular variation, 1, a hydromagnetic constraint: theory. J. Geomagn. Geoelectr. 17, 137–151.
Roperch, P., Chauvin, A., Lara, L., Moreno, H., 2015. Secular variation of the Earth's magnetic field and application to paleomagnetic dating of historical lava flows in Chile. Phys. Earth Planet. Inter. 242, 65–78.
Roperch, P., Chauvin, A., Le Pennec, J., Lara, L., 2014. Paleomagnetic study of juvenile basaltic-andesite clasts from Andean pyroclastic density current deposits. Phys. Earth Planet. Inter. 227, 20–29.
Shah, J., Koppers, A.A.P., Leitner, M., Leonhardt, R., Muxworthy, A.R., Heunemann, C., Bachtadse, V., Shley, J.A.D., Matzka, J., 2016. Paleomagnetic evidence for persistence of recurrence of geomagnetic main field anomalies in the South Atlantic. Earth Planet. Sci. Lett. 441, 113–124.
Tarduno, J.A., Watkeys, M.K., Huffman, T.N., Cottrell, D.C., Blackman, E.G., Wendt, A., Scribner, A.C., Wagner, C.L., 2015. Antiquity of the South Atantic Anomaly and evidence for top-down control on the geodynamo. Nat. Commun. 6, 7865. http://dx.doi.org/10.1038/ncomms8865.
Terra-Nova, F., Amit, H., Hartmann, G.A., Trindade, R.I.F., 2015. The time dependence of reversed archeomagnetic flux patches. J. Geophys. Res. 120 (2), 691–704. http://dx.doi.org/10.1002/2014JB011742.
Terra-Nova, F., Amit, H., Hartmann, G.A., Trindade, R.I.F., 2016. Using archaeomagnetic field models to constrain the physics of the core: robustness and preferred locations of reversed flux patches. Geophys. J. Int. 206 (3), 1890–1913. http://dx.doi.org/10.1093/gji/ggw248.
Thébault, E., Finlay, C.C., Beggan, C.D., Alken, P., Aubert, J., Barrois, O., Bertrand, F., Bondar, T., Boness, A., Brocco, L., Canet, E., Chambodut, A., Chulliat, A., Coïsson, P., Civet, F., Du, A., Fournier, A., Fratter, I., Gillet, N., Hamilton, B., Hamoudi, M., Hulot, G., Jager, T., Korte, M., Kuang, W., Lalanne, X., Langlais, B., Lger, J.-M., Lesur, V., Lowes, F.J., et al., 2015. International geomagnetic reference field: the twelfth generation. Earth Planets Space 67, 79. http://dx.doi.org/10.1186/s40623-015-0228-9.
Willis, P.W., Sreenivasan, B., Gubbins, D., 2007. Thermal core-mantle interaction: exploring regimes for 'locked' dynamo action. Phys. Earth Planet. Inter. 165, 83–92.